frontiers | Frontiers in Earth Science

TYPE Original Research
PUBLISHED 25 August 2022
DOI 10.3389/feart.2022.927695

OPEN ACCESS

EDITED BY
Shengyao Yu,
Ocean University of China, China

REVIEWED BY
Xinlu Hu,
China University of Geosciences Wuhan, China
Qiaoqiao Zhu,
Chinese Academy of Geological Sciences, China

*CORRESPONDENCE
You-Guo Li,
lyguo@cdut.edu.cn
Wen-Chang Li,
lwcyndd@163.com

SPECIALTY SECTION
This article was submitted to Petrology, a section of the journal Frontiers in Earth Science

RECEIVED 24 April 2022
ACCEPTED 12 July 2022
PUBLISHED 25 August 2022

CITATION
Liu H, Li Y-G, Li W-C, Li G-M, Ma D-F, Ouyang Y, Huang H-X, Zhang Z-L, Li T and Wu J-Y (2022), Petrogenesis of the late Cretaceous Budongla Mg-rich monzodiorite pluton in the central Lhasa subterrane, Tibet, China: Whole-rock geochemistry, zircon U-Pb dating, and zircon Lu-Hf isotopes.
Front. Earth Sci. 10:927695.
doi: 10.3389/feart.2022.927695

Petrogenesis of the late Cretaceous Budongla Mg-rich monzodiorite pluton in the central Lhasa subterrane, Tibet, China: Whole-rock geochemistry, zircon U-Pb dating, and zircon Lu-Hf isotopes

Hong Liu[1,2], You-Guo Li[1]*, Wen-Chang Li[2,3]*, Guang-Ming Li[2], Dong-Fang Ma[2], Yuan Ouyang[2], Han-Xiao Huang[2], Zhi-Lin Zhang[4], Tong Li[1] and Jun-Yi Wu[2,5,6]

[1]College of Earth Sciences, Chengdu University of Technology, Chengdu, China, [2]Chengdu Center, China Geological Survey, Chengdu, China, [3]College of Land and Resources Engineering, Kunming University of Science and Technology, Kunming, China, [4]The 5th Geological Team of Tibet Geological Exploration Bureau, Golmud, China, [5]Graduate School, Chinese Academy of Geological Sciences, Beijing, China, [6]Graduate School, China University of Geosciences, Beijing, China

Mg-rich monzodiorite are found in the Budongla gold ore district, Zhongba County, Xizang (Tibet) Autonomous Region, P.R. China. Studying the petrogenesis of this intermediate pluton can provide effective information to explore the geological evolution of the Lhasa terrane. One monzodiorite sample yielded a weighted mean $^{206}Pb/^{238}U$ age of 92.7 ± 1.1 Ma (mean square weighted deviation=0.33) using LA-ICP-MS zircon U-Pb dating, which represents the late phase of Late Cretaceous magmatism. The rock-forming minerals in the Budongla Mg-rich monzodiorite mainly include K-feldspar, plagioclase, quartz, biotite augite, and amphibole, and its accessory minerals mainly include magnetite, titanite, zircon, and apatite. The rocks are rich in K_2O+Na_2O and K_2O with medium contents of SiO_2, CaO, and $A1_2O_3$,, suggesting these rocks belong to the high-K calc-alkaline series. These rocks have high MgO, Fe_2O_3, and FeO, with high Mg# values and low DI, which implies they are Mg-rich intermediate intrusive rocks. The rocks are enriched in LREEs and LILEs and depleted in HREEs and HFSEs. They have negative Eu anomalies, no obvious negative Ce anomalies, and slightly negative $_{\varepsilon Hf}(t)$. We infer that the Budongla pluton is a high-K calc-alkaline metaluminous Mg-rich monzodiorite and intruded during the post-collisional period of the Lhasa and Qiangtang terranes.

KEYWORDS
central Lhasa terrane, Bangong-Nujiang, Budongla, postcollision, Mg-rich intermediate intrusive rocks

Introduction

The Lhasa terrane (LS), which is also known as the Gangdese-Nyainqentanglha terrane, is one of the main massifs of the Qinghai-Xizhang Plateau (Figures 1A,B), located between the Bangong-Nujiang suture zone (BNSZ) in the north and the Indus-Yarlung Zangbo suture zone (YZSZ) in the south (Pan et al., 2001; Yang et al., 2007; Pan et al., 2009; Liu et al., 2016; Liu et al., 2021a; Wang et al., 2022). The Lhasa terrane is critical for understanding the tectonic evolution of this Plateau, particularly with regard to early crustal thickening. Mesozoic to Cenozoic magmatic rocks are widely distributed in this block, which can provide insights into the geodynamic processes related to the growth of the Tibetan Plateau. The Lhasa terrane comprises three roughly parallel subterranes: the South Lhasa subterrane (SL), the Central Lhasa subterrane (CL), and the North Lhasa subterrane (NL) (Pan et al., 2009; Peng et al., 2013; Liu et al., 2020; Geng et al., 2021; Pan et al., 2022). Because of the evolution of the Bangong-Nujiang and Yarlung Zangbo Neo-Tethys during the Mesozoic to Cenozoic (Huang et al., 2017; Wu et al., 2017; Liu et al., 2019a, Liu et al., 2019b; Huang et al., 2020; Huang et al., 2021a), magmatic activity-related polymetallic deposits are widespread in this terrane (Zhao et al., 2013; Cai et al., 2015; Huang et al., 2018a, Huang et al., 2018b). Recent studies suggest that the Lhasa terrane was significantly thickened and elevated prior to the Cenozoic collision between India and Asia plates, probably associated with the Mesozoic collision between the Lhasa and Qiangtang blocks (Zhang et al., 2012; Yan and Zhang, 2020), or owing to the obduction of the fragments of the oceanic plateaus in the Bangong–Nujiang Ocean over the continental margins prior to the closure of the oceanic basin (Zhang et al., 2017).

To date, a large amount of post-collision-related Late Cretaceous (~90 Ma) magmatic activity has been found in the Central Lhasa subterrane (CL) (Figure 1C) (Liu et al., 2015; Gao, 2016; Li et al., 2016; Liu et al., 2018b; Wang et al., 2021a; Liu et al., 2022a), such as Zalongqiongwa (~91 Ma), Ga'erqiong (~88 Ma), Balaza (~90 Ma), Sebuta (~90 Ma), Xiangba (~90 Ma), Adang (~91 Ma), Zhuogapu (~85 Ma), Jingzhushan (~91 Ma), and Jiangla'zangzong (~86 Ma). This episode of magmatic activity is often accompanied by porphyry-epithermal or porphyry-skarn Cu(Au) or Au polymetallic mineralization. Several studies were carried out on the southern Lhasa terrane which suggest an archetype of Andean-style margin related to the northward subduction of the Neo-Tethyan Ocean before the India–Asia

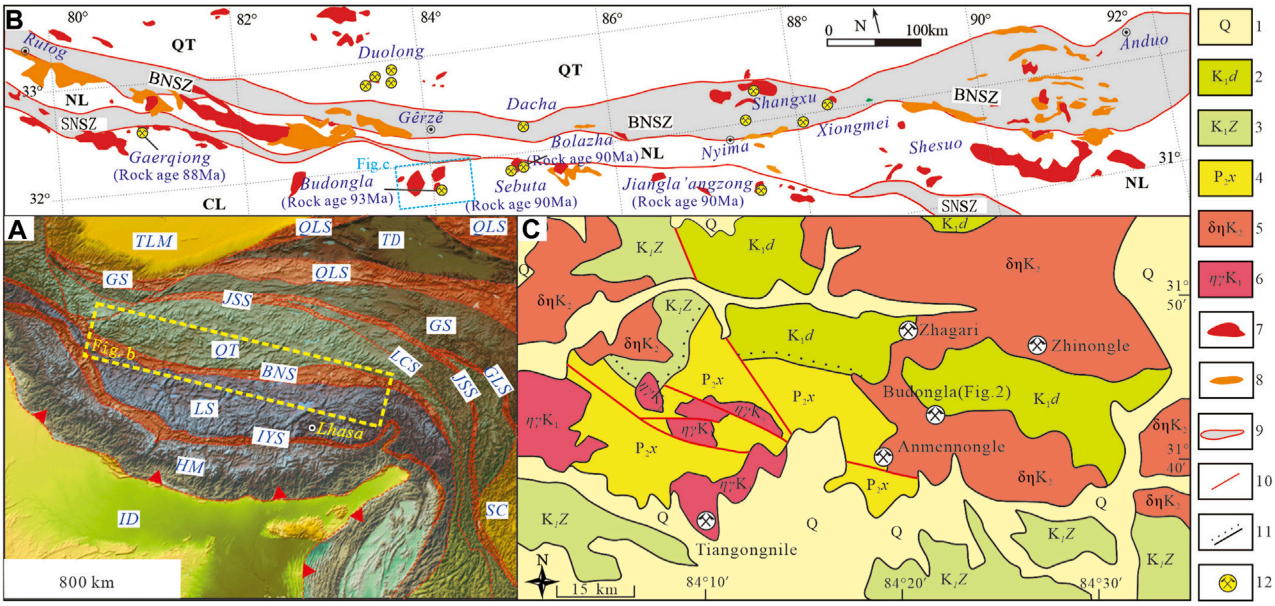

FIGURE 1
Regional geological and mineral maps [**(A)**, after Liu et al., 2015; **(B)**, after Tang et al., 2014; Liu et al., 2017; Liu et al., 2022b; Huang et al., 2021b; **(C)**, after Liu et al., 2021b] 1—Quaternary; 2—Lower Cretaceous Duoni Fm; 3—Lower Cretaceous Zenong Gr; 4—Lower Permian Xiala Gr; 5—Late Cretaceous monzodiorite; 6—Late Cretaceous monzogranite; 7—Ophiolite melange; 8—Cretaceous intrusive rocks; 9—Cretaceous volcanic rocks; 10—Fault; 11—Unconformity boundary; 12—Gold deposit (point); TLM—Tarim block; QLS—Qilian suture zone; WQS—Western Kunlun suture zone; EQS—Eastern Kunlun suture zone; TD—Tsaidam terranes; GS—Ganzi-Songpan terrane; JSS—Jinshajiang suture zone; GLS—Ganzi-Litang suture zone; LCS—Lancangjiang suture zone; QT—Qiangtang terrane; BNSZ—Bangong-Nujiang suture zone; LS—Lhasa terrane; NL—Northern Lhasa subterrane; SNSZ—Shiquanhe-Nam Co fault zone; CL—Central Lhasa subterrane; YZSZ—Yarlung-Tsangpo suture zone; HM—Himalayan terrane; SC—South China block; ID—Indian Plate.

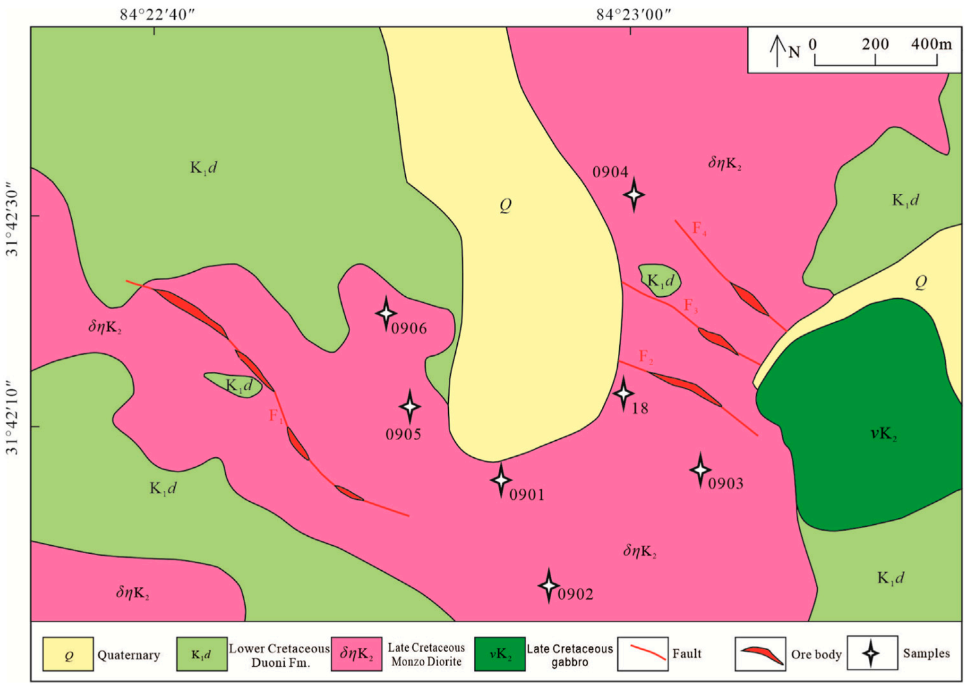

FIGURE 2
Geological map of the Budongla Gold deposit.

collision in the Early Cenozoic. However, the geological background of this Late Cretaceous magmatic activity is still controversial. Some researchers have proposed that the development of these Late Cretaceous magmatic rocks was related to the collision of the Qiangtang-Lhasa terrane (Gao et al., 2011; Wang et al., 2013); other scholars have proposed that these magmatic rocks are related to the northward subduction of the Yarlung Zangbo oceanic crust (Qin et al., 2019).

In this paper, whole-rock geochemistry, zircon U-Pb dating, and zircon Lu-Hf isotopes of the Late Cretaceous monzodiorite pluton (Figure 1C, Figure 2) in the Budongla gold deposit of Zhongba County in the Central Lhasa subterrane are studied. The age of the monzodiorite pluton is precisely determined, and the source area and tectonic setting of its parent magma are discussed.

Geological background

The monzodiorite pluton samples were collected from the Budongla gold district. This gold district is located at the junction of Zhongba County and Gaize County in the Tibet Autonomous Region, P.R. China, which belongs to the western part of the Central Lhasa subterrane (Figure 1). The main stratigraphic units exposed in this region include the Lower Cretaceous Duoni Formation, which consists of limestone and sandstone with some interbedded volcanic rocks; the Lower Cretaceous Zenong Group, which mainly consists of intermediate-felsic volcanic rocks and pyroclastic rocks; and the Middle Permian Xiala Formation, which consists of marble and limestone (Figure 1C). From the perspective of structural deformation characteristics, the structure is mainly compressional deformation, with twists, strike-slip displacements, and extensional structures (Figure 1C). The lithologies of Mesozoic-Cenozoic magmatic rocks is mainly monzodiorite, monzogranite, and biotite granite. They intruded into the Doni Formation and Xiala Formation in the form of composite stocks, batholiths, and dikes and formed skarnization and hornfelsization zones of a certain scale. There is a series of copper-gold hydrothermal deposits related to Late Cretaceous intermediate magmatism (Figure 1C), such as Tiangongnile, Zhagari, Anmennongle, and Zhinongle (Huang et al., 2012a, Huang et al., 2012b; Ouyang et al., 2016; Li et al., 2017).

The stratigraphic units exposed in the Budongla gold ore district mainly include the Lower Cretaceous Doni Formation and the Quaternary system (Figure 2). The Doni Formation is widely distributed on the northern and southern sides of the ore district. It is a set of littoral and

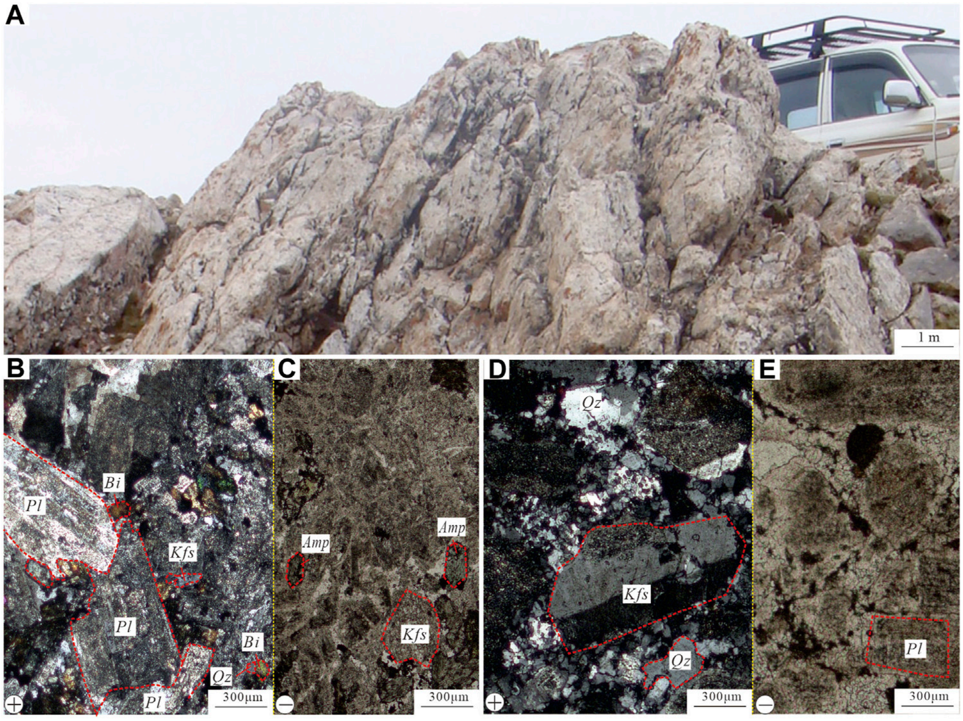

FIGURE 3
Petrographic characteristics of the rocks in Budongla. **(A,B)**: The field outcrops of the mmonzodiorite; **(C–E)**: Microphotographs in plane polarized light (-) and perpendicular polarized light (+) of the monzodiorite. Pl: plagioclase; Kfs: K-feldspar; Qz: Quartz; Bi: Biotite; Amp: Amphibolites.

shallow marine clastic sedimentary formations. The Quaternary is mainly developed in the river valley and consists of alluvial proluvial gravel layers, gravelly sand and clay layers, and residual slope sand gravel layers. The structures in the ore district are mainly NW-trending compressional and torsional faults, which are slightly wave-shaped, and the width of the faults vary from 1 to 5 m (Figure 2). The Late Cretaceous monzodiorite pluton is exposed in a large area in the Budongla mining area and intruded into the sandstone of the Lower Cretaceous Doni Formation. The exposed area of the Late Cretaceous monzodiorite pluton in the mining area is more than 2 km^2, accounting for approximately 1/2 of the total area of the ore district (Figures 2, 3). The monzodiorite is gray with a medium-to coarse-grained porphyritic structure (Figure 3). And the grain size of the main mineral phenocrysts is 2–8 mm. Major minerals are K-feldspar (25%±), plagioclase (45%±), amphibole (15%±), quartz (5%±), augite (3%±), and biotite (3%±). Accessory minerals include magnetite (<1%), titanite (<1%), zircon (<1%), and apatite (<1%). Late Cretaceous gabbro is located in the western part of the ore district, with an exposed area of approximately 0.2 km^2 (Figure 2). At present, several hydrothermal vein-type gold (mineralized) bodies have been found in fracture zones within the pluton (Figure 2). According to the exploration report The fifth Geological Team of Tibet Geological Exploration Bureau, the main ore belt is located in the west of Budongla gold ore district, which is composed of four ore bodies with a grade of 1–11.91 g/t (with the average grade of 7.12 g/t) and a thickness of 1.55–4.51 m (with the average grade of 2.10 m).

Sampling and analytical methods

Seven samples were collected from the Budongla monzodiorite pluton (Figure 1C). All samples were sent for thin section observation and whole-rock major and trace element geochemical analyses, and one of them was used for LA-ICP-MS zircon U-Pb dating and Lu-Hf isotope analyses. Major and trace element analyses were conducted by the XRF (Primus Ⅱ, Rigaku, Japan) and ICP-MS (Agilent 7700e) methods in the Wuhan Sample Solution Analytical Technology Co., Ltd. We performed zircon cathodoluminescence (CL) imaging at Wuhan Sample

TABLE 1 Major element compositions of monzodiorite in the Budongla gold district.

Element	Unit	BDL09-1	BDL09-2	BDL09-3	BDL09-4	BDL09-5	BDL09-6	BDL18
SiO_2	wt%	55.19	55.56	55.75	55.79	54.69	55.28	54.93
TiO_2	wt%	0.93	0.96	1.02	1.06	0.92	0.96	1.00
Al_2O_3	wt%	16.52	16.69	15.54	15.45	16.79	16.59	16.51
Fe_2O_3	wt%	5.04	4.86	5.05	4.14	5.90	5.34	5.18
FeO	wt%	1.66	1.69	1.59	2.55	1.02	1.46	1.72
MnO	wt%	0.11	0.10	0.12	0.12	0.11	0.10	0.12
MgO	wt%	4.92	4.78	5.22	5.54	5.24	4.99	5.20
CaO	wt%	6.75	6.56	7.13	7.48	7.12	6.90	6.94
Na_2O	wt%	3.38	3.47	3.13	3.11	3.31	3.18	3.31
K_2O	wt%	2.67	2.71	2.73	2.64	2.43	2.78	2.68
P_2O_5	wt%	0.52	0.50	0.51	0.52	0.55	0.54	0.53
Loss	wt%	1.94	1.74	1.83	1.38	1.76	1.56	1.54
Total	wt%	99.63	99.62	99.62	99.78	99.84	99.68	99.64
FeOT	wt%	6.19	6.06	6.13	6.28	6.33	6.26	6.32
σ43	mass ratio	2.84	2.90	2.66	2.49	2.68	2.77	2.73
DI	volume ratio	50.52	51.65	49.09	48.44	48.41	49.68	49.76
Mg#	mol ratio	58.60	58.43	60.20	61.15	59.63	58.67	59.01
A/NK	mol ratio	1.96	1.93	2.00	1.94	2.07	2.01	1.98
A/CNK	mol ratio	0.80	0.81	0.78	0.72	0.80	0.80	0.79
La	wt×10^{-6}	67.1	62.0	64.2	61.9	66.1	64.4	64.3
Ce	wt×10^{-6}	130	116	125	121	128	126	124
Pr	wt×10^{-6}	15.0	13.4	13.4	13.9	14.8	14.5	14.7
Nd	wt×10^{-6}	55.6	49.3	53.2	50.7	55.4	53.7	53.0
Sm	wt×10^{-6}	8.61	7.82	8.38	8.18	8.58	8.49	8.44
Eu	wt×10^{-6}	2.03	1.87	1.91	1.79	1.99	1.96	1.96
Gd	wt×10^{-6}	6.84	6.08	6.41	6.27	6.49	6.44	6.45
Tb	wt×10^{-6}	0.869	0.802	0.835	0.828	0.864	0.845	0.826
Dy	wt×10^{-6}	4.36	4.02	4.25	4.15	4.29	4.35	4.22
Ho	wt×10^{-6}	0.741	0.662	0.736	0.711	0.732	0.743	0.720
Er	wt×10^{-6}	2.09	1.96	2.02	1.97	2.07	2.06	2.06
Tm	wt×10–6	0.301	0.270	0.277	0.274	0.282	0.282	0.281
Yb	wt×10^{-6}	1.91	1.65	1.74	1.73	1.75	1.80	1.78
Lu	wt×10^{-6}	0.250	0.242	0.246	0.245	0.244	0.254	0.249
Y	wt×10^{-6}	22.1	20.2	21.5	21.1	21.7	21.6	21.4
Rb	wt×10^{-6}	127	125	122	117	130	121	126
Ba	wt×10^{-6}	612	589	546	540	477	605	562
Th	wt×10^{-6}	21.0	17.1	17.7	18.3	16.9	17.1	18.3
U	wt×10^{-6}	3.25	2.67	3.19	3.86	2.52	3.18	3.08
Nb	wt×10^{-6}	12.0	12.2	12.6	16.1	10.4	11.6	12.5
Ta	wt×10^{-6}	0.784	0.770	0.777	0.981	0.603	0.751	0.779
Pb	wt×10^{-6}	20.7	17.2	18.3	18.0	15.8	20.1	18.0
Sr	wt×10^{-6}	982	941	933	904	901	951	926
Zr	wt×10^{-6}	118	131	125	131	106	126	120
Hf	wt×10^{-6}	3.16	3.23	3.01	3.33	2.72	3.26	3.15
Ga	wt×10^{-6}	20.3	20.4	20.1	19.4	20.8	19.8	20.2
ΣREE	wt×10^{-6}	295	266	282	274	291	286	283
LREE/HREE	mass ratio	16.01	15.95	16.11	15.95	16.42	16.05	16.07
δEu	mass ratio	0.79	0.80	0.77	0.74	0.78	0.78	0.78
δCe	mass ratio	0.95	0.93	0.98	0.96	0.95	0.96	0.94

Notes: A/CNK=Al_2O_3/(CaO+Na_2O+K_2O) (molar ratio); A/NK= Al_2O_3/(Na_2O+K_2O) (molar ratio); Mg#=Mg/(Mg+Fe) (molar ratio); σ43=(Na_2O+K_2O)2/(SiO_2-43); δEu = 2 × EuN/(SmN+GdN); δCe=2 × CeN/(LaN+PrN); DI= Quartz+Orthoclase+Albite+Nepheline+ Leucite+K-feldspar, from CIPW, calculating values.

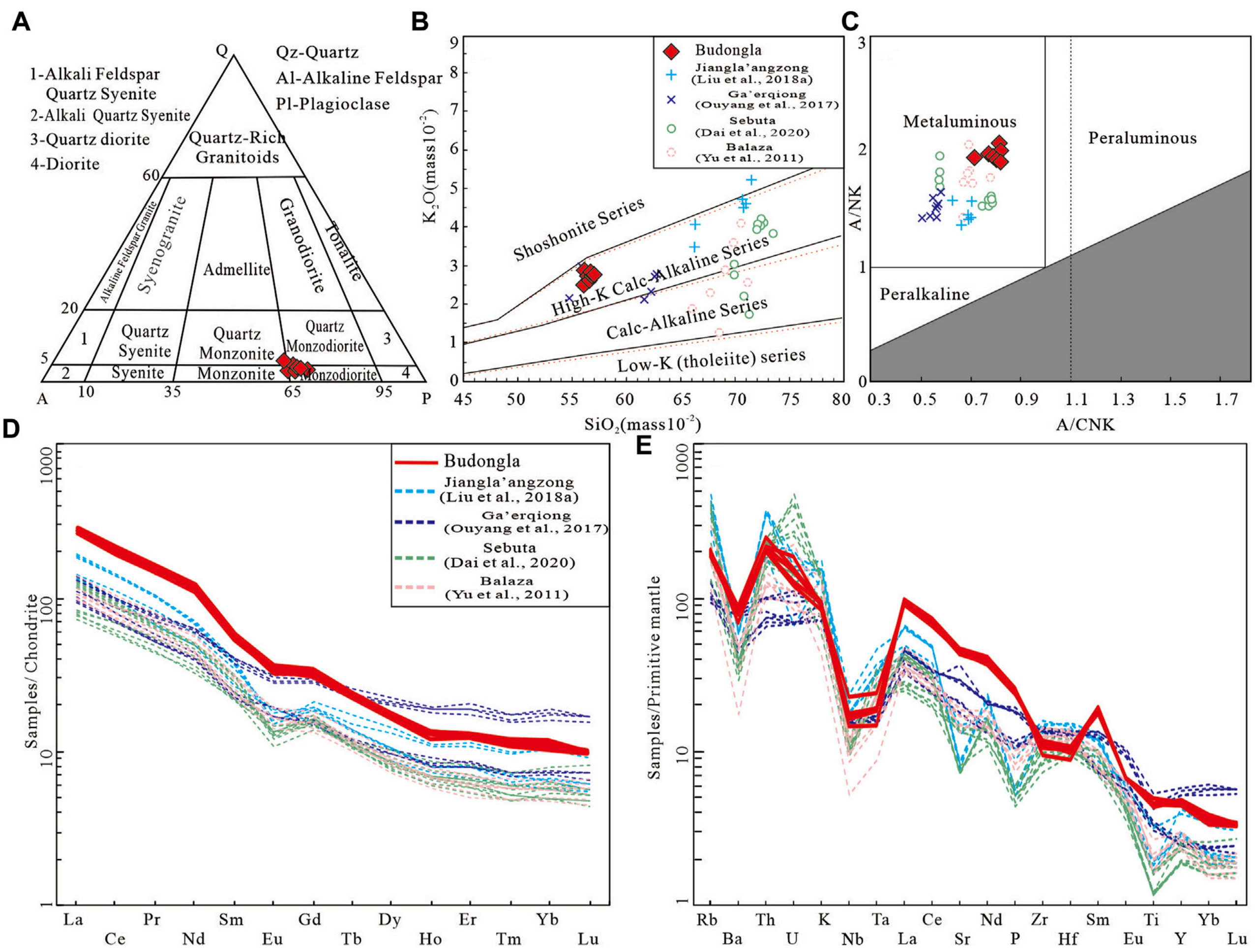

FIGURE 4
Geochemical diagrams of major elements. **(A)**, QAP Plots of rock (base map after LeMaitre, 2002); **(B)**, K_2O vs. SiO_2 Plots (base map after Middlemost, 1994); **(C)**, A/NK vs. A/CNK Plots (base map after Maniar and Piccoli, 1989); **(D)**, Chondrite-normalised REE patterns (The normalizing values for REE are from Sun and McDonough and Sun, 1995); **(E)**, Mantle-normalised multi-element diagrams. (The normalizing values for REE and trace elements are from Sun and McDonough, 1989; McDonough and Sun, 1995).

Solution Analytical Technology Co., Ltd. Wuhan, China, using an analytical scanning electron microscope (JSM-IT100) connected to a GATAN MINICL system. The analytical conditions included a 10.0–13.0 kV electric field voltages and an 80–85 μA current on a tungsten filament. Zircon U-Pb dating, zircon trace element analysis, and zircon Lu-Hf isotope analysis were simultaneously conducted by LA-MC-ICP-MS at the Wuhan Sample Solution Analytical Technology Co., Ltd. The spot size and frequency of the laser were set to 32 μm, and the energy density of laser ablation was ~7.0 J/cm2 in this study. Zircon 91,500. Zircon GJ-1, and glass NIST610 were used as external standards for U-Pb dating and trace element calibration, respectively. Each analysis involved a background acquisition of approximately 20–30 s followed by 50 s of data acquisition for each sample. ICPMSDataCal, an Excel-based software, was used to perform offline data selection, the integration of background and analyzed signals, time-drift corrections, and quantitative calibration for trace element analysis and U-Pb dating. Concordia diagrams and weighted mean calculations were made using Isoplot/Ex_ver 4.15 software.

Results

Major and trace elements

The whole-rock major and trace element geochemical data are listed in Table 1. The rocks are rich in K_2O+Na_2O (5.75 wt% ~6.18 wt%) and K_2O (2.44 wt% ~2.78 wt%), have medium

10.3389/feart.2022.927695

TABLE 2 LA-ICP-MS zircon U-Pb ages of monzodiorite in the Budongla gold district.

Spots	Pb × 10^{-6}	Th × 10^{-6}	U × 10^{-6}	Th/U	$^{207}Pb/^{206}Pb$	1σ	Isotope ratio		$^{206}Pb/^{238}U$	1σ	$^{207}Pb/^{206}Pb$	1σ	Age (Ma)		$^{206}Pb/^{238}U$	1σ	Con %
							$^{207}Pb/^{235}U$	1σ					$^{207}Pb/^{235}U$	1σ			
91500std	19.18	31.5	88.8	0.36	0.0728	0.0025	1.7989	0.0604	0.1791	0.0023	1,009	69	1,045	22	1,062	13	98
91500std	19.23	31.3	88.7	0.35	0.0770	0.0026	1.9015	0.0625	0.1792	0.0022	1,120	67	1,082	22	1,063	12	98
GJ-1	34.39	9.37	324	0.03	0.0587	0.0016	0.7907	0.0211	0.0973	0.0010	554	59	592	12	599	6	98
GJ-1	34.87	9.39	329	0.03	0.0592	0.0016	0.7988	0.0222	0.0975	0.0010	576	56	596	13	600	6	99
BDL18-1	15.1	177	349	0.51	0.0523	0.0059	0.0973	0.0084	0.0147	0.0004	298.2	224.0	94.3	7.7	93.9	2.5	99
BDL18-2	46.3	712	640	1.11	0.0510	0.0053	0.0988	0.0088	0.0147	0.0003	242.7	207.4	95.6	8.1	94.4	2.1	98
BDL18-3	13.5	155	321	0.48	0.0481	0.0019	0.0970	0.0029	0.0146	0.0001	101.9	87.0	94.0	2.7	93.3	0.8	99
BDL18-4	15.5	146	701	0.21	0.0448	0.0020	0.0886	0.0039	0.0143	0.0002	—	—	86.2	3.7	91.6	1.0	94
BDL18-5	30.7	417	474	0.88	0.0520	0.0034	0.1048	0.0065	0.0147	0.0002	287.1	137.0	101.2	6.0	93.8	1.2	92
BDL18-6	39.0	548	667	0.82	0.0524	0.0038	0.0991	0.0066	0.0144	0.0002	301.9	154.6	96.0	6.1	92.3	1.4	96
BDL18-7	33.3	452	506	0.89	0.0457	0.0021	0.0947	0.0031	0.0146	0.0002	—	—	91.9	2.9	93.6	1.0	98
91500std	18.64	31.0	87.1	0.36	0.0750	0.0027	1.8592	0.0665	0.1800	0.0023	1,133	73	1,067	24	1,067	13	99
91500std	19.03	31.7	88.7	0.36	0.0748	0.0027	1.8412	0.0664	0.1783	0.0022	1,065	79	1,060	24	1,058	12	99
BDL18-8	14.4	183	202	0.91	0.0462	0.0029	0.0927	0.0055	0.0146	0.0002	5.7	137.0	90.0	5.1	93.6	1.0	96
BDL18-9	14.5	184	203	0.91	0.0461	0.0031	0.0998	0.0061	0.0142	0.0002	400.1	49.1	96.6	5.6	90.8	1.1	93
BDL18-10	41.3	584	594	0.98	0.0469	0.0019	0.0955	0.0033	0.0146	0.0001	42.7	95.4	92.7	3.0	93.5	0.8	99
BDL18-11	18.3	237	387	0.61	0.0463	0.0022	0.0938	0.0044	0.0146	0.0001	13.1	110.2	91.1	4.1	93.7	0.8	97
BDL18-12	33.0	462	526	0.88	0.0504	0.0032	0.1002	0.0061	0.0145	0.0002	216.7	135.2	96.9	5.6	92.7	1.1	95
BDL18-13	11.1	151	186	0.81	0.0482	0.0078	0.0935	0.0123	0.0146	0.0006	109.4	317.6	90.7	11.4	93.2	3.5	97
BDL18-14	27.6	356	537	0.66	0.0499	0.0069	0.0980	0.0108	0.0147	0.0006	190.8	276.8	95.0	10.0	94.2	3.7	99
BDL18-15	28.1	373	441	0.85	0.0550	0.0084	0.0978	0.0117	0.0145	0.0004	413.0	287.9	94.7	10.8	92.9	2.7	98
BDL18-16	77.2	846	2,229	0.38	0.0546	0.0055	0.1033	0.0096	0.0145	0.0003	398.2	227.7	99.8	8.8	92.6	1.9	92
91500std	20.41	33.8	94.2	0.36	0.0741	0.0025	1.8286	0.0629	0.1790	0.0025	1,043	67	1,056	23	1,061	14	99
91500std	19.43	32.1	89.7	0.36	0.0757	0.0025	1.8718	0.0624	0.1794	0.0024	1,087	66	1,071	22	1,064	13	99
BDL18-17	30.6	410	658	0.62	0.0545	0.0055	0.1019	0.0095	0.0139	0.0002	390.8	229.6	98.5	8.8	89.0	1.6	89

(Continued on following page)

10.3389/feart.2022.927695

TABLE 2 (*Continued*) LA-ICP-MS zircon U-Pb ages of monzodiorite in the Budongla gold district.

Spots	Pb × 10^{-6}	Th × 10^{-6}	U × 10^{-6}	Th/U	$^{207}Pb/^{206}Pb$	1σ	Isotope ratio		$^{206}Pb/^{238}U$	1σ	$^{207}Pb/^{206}Pb$	1σ	Age (Ma)		$^{206}Pb/^{238}U$	1σ	Con %
							$^{207}Pb/^{235}U$	1σ					$^{207}Pb/^{235}U$	1σ			
BDL18-18	16.1	219	303	0.72	0.0565	0.0043	0.1037	0.0074	0.0138	0.0003	472.3	165.7	100.2	6.8	88.5	1.7	87
BDL18-19	24.6	339	581	0.58	0.0547	0.0041	0.1102	0.0088	0.0146	0.0003	398.2	170.4	106.2	8.0	93.7	1.9	87
BDL18-20	24.4	334	576	0.58	0.0491	0.0035	0.0924	0.0065	0.0141	0.0003	153.8	168.5	89.8	6.1	90.0	1.7	99
BDL18-21	23.2	305	439	0.69	0.0552	0.0037	0.1062	0.0070	0.0141	0.0003	420.4	151.8	102.5	6.5	90.3	1.8	87
BDL18-22	23.3	305	440	0.69	0.0527	0.0037	0.1041	0.0071	0.0147	0.0003	316.7	162.9	100.5	6.6	94.0	1.8	93
GJ-1	35.80	9.61	336	0.03	0.0595	0.0017	0.8029	0.0226	0.0976	0.0012	587	66	598	13	600	7	99
GJ-1	35.68	9.63	333	0.03	0.0593	0.0018	0.8015	0.0246	0.0974	0.0011	589	60	598	14	599	6	99
91500std	20.28	33.9	93.2	0.36	0.0736	0.0027	1.8150	0.0660	0.1792	0.0024	1,031	76	1,051	24	1,062	13	98
91500std	19.82	32.9	91.3	0.36	0.0761	0.0025	1.8854	0.0653	0.1792	0.0028	1,098	67	1,076	23	1,062	15	98

TABLE 3 LA-ICP-MS zircon Lu-Hf isotopes compositions of monzodiorite in the Budongla gold district.

Spots	t (Ma)	^{176}Yb/^{177}Hf	^{176}Lu/^{177}Hf	^{176}Hf/^{177}Hf	2σ	^{176}Hf/^{177}Hf(t)	$\varepsilon_{Hf}(0)$	$\varepsilon_{Hf}(t)$	T_{DM}(Ma)	TDM2 (Ma)	$f_{Lu\text{-}Hf}$
BDL18-1	93.9	0.050478	0.001219	0.282,706	0.000026	0.282,704	−2.3	−0.4	778	1,176	−0.96
BDL18-2	94.4	0.055745	0.001406	0.282,617	0.000031	0.282,614	−5.5	−3.5	909	1,377	−0.96
BDL18-3	93.3	0.170,006	0.003642	0.282,678	0.000096	0.282,671	−3.3	−1.5	875	1,249	−0.89
BDL18-4	91.6	0.019052	0.000432	0.282,669	0.000716	0.282,668	−3.6	−1.7	813	1,257	−0.99
BDL18-5	93.8	0.027366	0.000582	0.282,628	0.000317	0.282,627	−5.1	−3.1	873	1,348	−0.98
BDL18-6	92.3	0.029551	0.000620	0.282,562	0.000253	0.282,561	−7.4	−5.4	966	1,497	−0.98
BDL18-7	93.6	0.032434	0.000696	0.282,645	0.000708	0.282,644	−4.5	−2.5	852	1,311	−0.98
BDL18-8	93.6	0.024269	0.000537	0.282,640	0.000370	0.282,639	−4.7	−2.7	856	1,322	−0.98
BDL18-9	90.8	0.029035	0.000620	0.282,663	0.000222	0.282,662	−3.9	−1.9	826	1,272	−0.98
BDL18-10	93.5	0.026351	0.000564	0.282,619	0.000033	0.282,618	−5.4	−3.4	887	1,370	−0.98
BDL18-11	93.7	0.038390	0.000786	0.282,602	0.000165	0.282,601	−6.0	−4.0	915	1,408	−0.98
BDL18-12	92.7	0.022271	0.000467	0.282,654	0.000156	0.282,654	−4.2	−2.2	834	1,290	−0.99
BDL18-13	93.2	0.020905	0.000467	0.282,617	0.000332	0.282,617	−5.5	−3.5	886	1,372	−0.99
BDL18-14	94.2	0.016626	0.000345	0.282,662	0.000192	0.282,661	−3.9	−1.9	822	1,272	−0.99
BDL18-15	92.9	0.028649	0.000576	0.282,656	0.000311	0.282,655	−4.1	−2.1	834	1,286	-0.98
BDL18-16	92.6	0.028953	0.000588	0.282,685	0.000367	0.282,684	−3.1	−1.1	794	1,221	−0.98
BDL18-17	89.0	0.040672	0.000796	0.282,617	0.000120	0.282,615	−5.5	−3.6	895	1,378	−0.98
BDL18-18	88.5	0.030673	0.000633	0.282,606	0.000632	0.282,605	−5.9	−4.0	906	1,402	−0.98
BDL18-19	93.7	0.044316	0.000868	0.282,644	0.001298	0.282,642	−4.5	−2.5	858	1,315	−0.97

Notes: $_{\varepsilon Hf}(0)=(^{176}Hf/^{177}Hf/(^{176}Hf/^{177}Hf)_{CHUR}, 0^{-1}) \times 10{,}000$; $_{\varepsilon Hf}(t)=[^{176}Hf/^{177}Hf\text{-}(^{176}Lu/^{177}Hf)_S \times (e^{\lambda t}\text{-}1)]/[(^{176}Hf/^{177}Hf)_{CHUR}, 0\text{-} (^{176}Lu/^{177}Hf)_{CHUR}\times (e^{\lambda t}\text{-}1)]\text{-}1) \times 10{,}000$; $[(^{176}Hf/^{177}Hf) i=^{176}Hf/^{177}Hf\text{-}(^{176}Lu/^{177}Hf)_S\times(e^{\lambda t}\text{-}1)]\text{-}1$; $T_{DM2}=T_{DM1}\text{-}(T_{DM1}\text{-}t)\ (f_{CC}\text{-}f_{Lu/Hf})/(f_{CC}\text{-}f_{DM})$; $f_{Lu}/H_f=^{176}Lu/^{177}Hf/(^{176}Lu/^{177}Hf)_{CHUR}\text{-}1$; $(^{176}Lu/^{177}Hf)_{CHUR}$, 0.0332, $(^{176}Hf/^{177}Hf)_{CHUR}$, 0=0.282,772 (Blichert-Toft and Albaréde, 1997); $(^{176}Lu/^{177}Hf)$DM, 0.0384, $(^{176}Hf/^{177}Hf)_{DM}$, 0.28325(Griffin et al., 2000); f_{CC}=−0.55, f_{DM}, 0.16, $\lambda=1.867 \times 10^{-11}$ years-1(Griffin et al., 2002).

contents of SiO_2 (54.85 wt% ~55.79 wt%), CaO (6.56 wt% ~7.48 wt%), and $A1_2O_3$ (15.45 wt% ~16.79 wt%), and have Rittmann indices (σ43) ranging from 2.49 to 2.90. The A/CNK values and A/NK range from 0.72 to 0.81 and 1.93 to 2.07, respectively, and the samples thus belong to the high-K calc-alkaline series (Table 1; Figure 4). The rocks have high MgO (4.92 wt%~5.54 wt%), Fe_2O_3 (4.14 wt%~5.90 wt%), FeO (1.02 wt%~2.55 wt%), the Mg# values of 58.43–61.15, and DI values of 48.41–51.65, implying they are Mg-rich intrusive rocks.

Figures 4D,E show that the Budongla monzodiorite pluton is enriched in light REEs (LREEs) (L_{REE}/H_{REE}: 15.95–16.42) and large ion lithophile elements (LILEs), while relatively depleted in heavy REEs (HREEs) and high field strength elements (HFSEs), and has negative Eu anomalies (δEu=0.74–0.80), no obvious negative Ce anomalies (δCe=0.93–0.98) (Table 1; Figure 4D).

Zircon U–Pb ages and Lu-Hf isotope compositions

The zircon U-Pb and Lu-Hf isotope data are listed in Tables 2, 3. Representative cathodoluminescence images of the zircons are shown in Figure 4A. All zircon Th/U ratios are higher than 0.30 (Th/U=0.5–0.9) (Table 2), and most of the zircon particles display relatively idiomorphic crystal morphology and clear oscillatory growth zoning in cathodoluminescence images (Figure 5A), which indicates that the zircons in this study are of magmatic origin (Figure 5C; Hoskin and Black, 2000; Grimes etal et al., 2007). The zircon data yield a concordia age of 92.7 ±1.1 Ma (*n*=22, MSWD=0.33) (Figures 5A,B), which suggests that the Budongla monzodiorite pluton was emplaced in the Late Cretaceous. We analyzed 19 zircon grains for Lu-Hf isotopes, as shownedin Table 3.

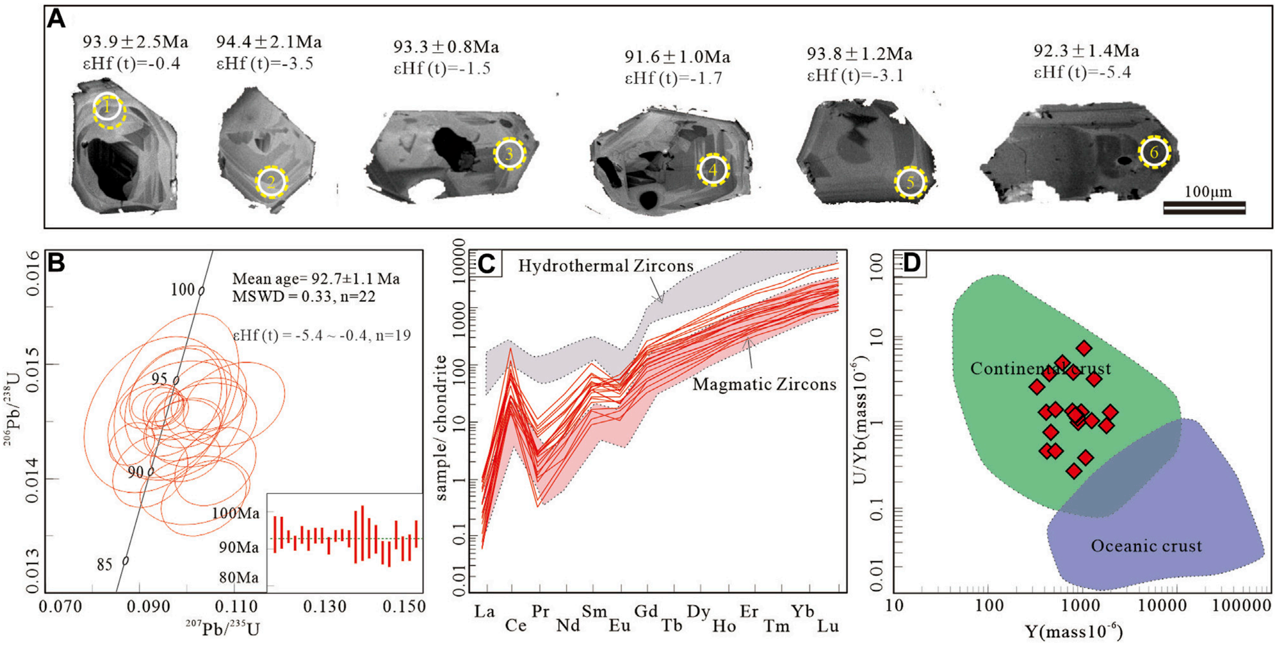

FIGURE 5
Diagrams of Zircon U-Pb geochronology. **(A)** Cathodoluminescence (CL) images of representative zircon grains; **(B)** zircon U-Pb concordia diagrams and weighted mean ages; **(C)** chondrite-normalized REE patterns of zircons (based on Hoskin, 2005); and **(D)** discriminant diagrams with differentcry stallization setting zircon fields (base on Grimes etal et al., 2007) for the Xiabie Co granite.

The zircons have low $^{176}Lu/^{177}Hf$ ratios of 0.000345–0.0036421 and $^{176}Hf/^{177}Hf$ ratios of 0.282,562–0.282,706. We calculated the initial $^{176}Hf/^{177}Hf$ ratio and $_{\varepsilon Hf}(t)$ values based on the zircon U-Pb ages, as showned in Table 3 and Figure 6. The T_{DM2} (two-stage Hf model ages) range from 1,176 to 1,497 Ma, and the $_{\varepsilon Hf}(t)$ values of the zircons in the Budongla monzodiorite pluton range from −5.4 to −0.4.

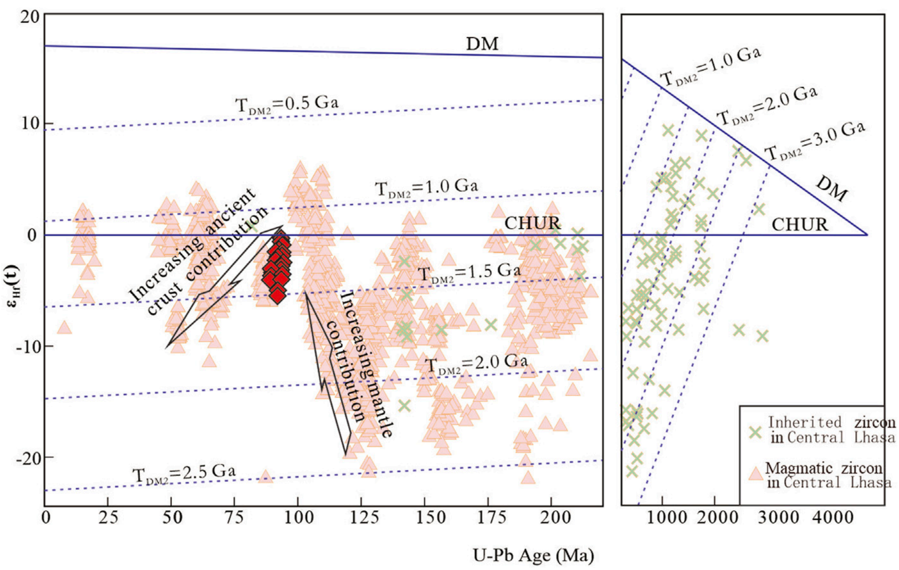

FIGURE 6
$_{\varepsilon Hf}(t)$ vs. U-Pb ages Plots of zircons. (The Central Lhasa values from Yu et al., 2011; Wang et al., 2012; Meng et al., 2014; Hou et al., 2015; Zhao et al., 2011; Liu et al., 2018a; Cao et al., 2019; DM: Depleted Mantle; CHUR: Chondrite uniform reservoir).

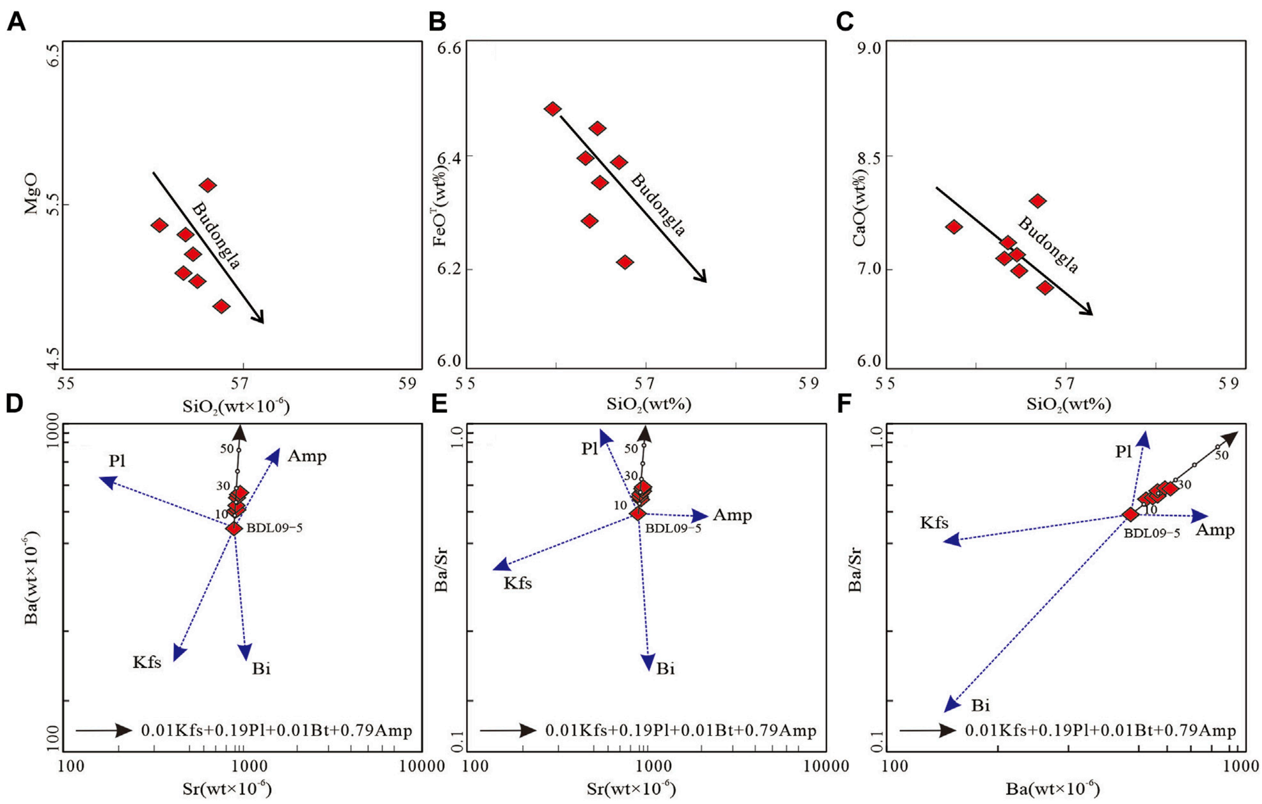

FIGURE 7
Huck diagram. **(A-C)** Element scatter diagrams; and **(D-F)** Quantitative simulation diagrams of crystallization differentiation.

Discussion

Magmatic source

As mentioned above, the Budongla monzodiorite pluton belongs to the metaluminous and high-K calc-alkaline Mg-rich magmatic rock series (Figures 4B,C). Different from other Late Cretaceous intermediate-felsic intrusive rocks in the Central Lhasa subterrane, the Budongla monzodiorite pluton has no obvious depletion in Sr, P, and Ti (Figure 4D). Therefore, there may have been no obvious fractional crystallization of phosphorus-containing minerals (such as apatite) and titanium-containing minerals (such as rutile) in the Budongla monzodiorite pluton. However, the negative Eu anomalies (Table 1; Figure 4D), the negative correlations between FeO^T, Cao, MgO, and SiO_2 (Figures 7A–C), and the obvious depletions in Ba and Ta (Figure 4E), indicate that there was a certain amount of fractional crystallization of plagioclase and iron magnesium minerals (such as amphibole) during magmatic evolution. This interpretation is supported by quantitative modeling of fractional crystallization (Figures 7D–F), which shows that the Budongla monzodiorite can be interpreted as forming through 0%–30% fractional crystallization of 0.01% K-feldspar +0.19% plagioclase +0.01% biotite +0.79% amphibole, and the degree of crystal differentiation is very low. The differentiation coefficient (DI=48.41–51.65) and FeO^T/MgO contents of the Budongla monzodiorite pluton are relatively low (Table 1; Figure 7), which indicates that the magma haven't experience a strong crystallization differentiation process, so it is unlikely to have been the product of crystallization of coeval basaltic magma.

The zircon trace elements have the characteristics of crustal sources (Figure 5D), and the Rb/Y-Nb diagram shows that the rocks have a trend of crustal contamination and obvious depletion in Nb (Figure 4B, Nb_N=14.6–24.6), which shows that the Budongla monzodiorite has crustal components. The Rb/Sr ratio of mongzodiorite in budongla (0.129–0.144) is much higher than the average value of primitive mantle (0.029, Sun and MchDonough, 1989), but close to the average value of continental crust (0.123, Taylor and McLennan, 1985). The rocks are characterized by enrichment of LILEs such as Rb, K, Th, and U, and relative loss of HFSEs such as Nb, Ta, P, and Ti, suggesting that the crust source material makes a great contribution to the source area (McKenzie and Bickle, 1988). The negative εHf(t) (−5.4~−0.4) (Figure 6) and old zircon Lu-Hf isotope two-stage model ages (T_{DM2}=1,176–1,497 Ma) suggest a

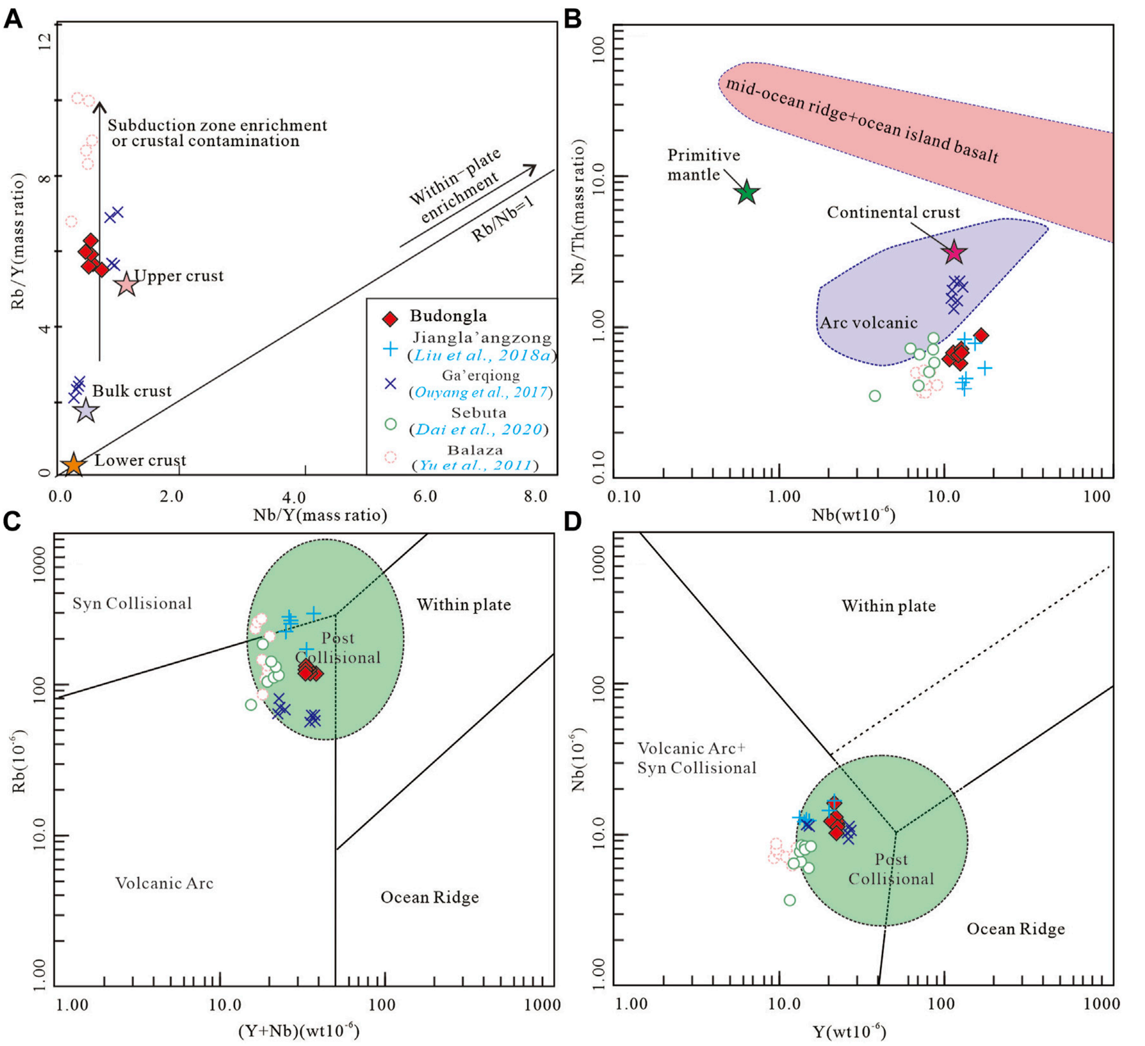

FIGURE 8
Tectonic discrimination diagrams. [**(A,B)**, Basemap after Pearce et al., 1984; **(C,D)**, Basemap after Boztuğ et al., 2007].

contribution of less radiogenic material was involved in the origin of monzodiorites or old crust (Scherer et al., 2000; Griffin et al., 2002). This could be crustal contamination during emplacement, or partial melting of the crust, which is consistent with the results of trace element analysis (Nb, Rb, Sr, Th, and U, etc.) But the arc volcanic rock characteristics of Ce/Pb, Ce, Nb/Th, and Nb (Figures 8A,B) show that the Budongla pluton is unlikely to have formed from pure crustal sources. In the Central Lhasa subterrane, from the early Cretaceous (~125 Ma) to the late Cretaceous (~90 Ma), the continuous increase of zircon $_{\varepsilon Hf}$(t) values also suggest that the continuous increasing mantle contribution to Cretaceous magmatic rock (Figure 6). In addition, the high Mg# and MgO also indicate that the Budongla Mg-rich monzodiorite has some mantle-derived derived components.

In summary, we infer that the Budongla Mg-rich monzodiorite pluton was generated by increasing the contribution of mantle sources during crustal remelting.

Tectonic environment

The development of the northern and middle parts of the Lhasa terrane is controversial. Some scholars have proposed that this Late Cretaceous magmatic activity was related to the collision of the Qiangtang-Lhasa terranes (Gao et al., 2011; Wang et al., 2013; Li et al., 2020; Wang et al., 2021b); other scholars have also suggested that the northward subduction of the Yarlung Zangbo Neotethys Ocean involved low-angle subduction and an increase in subduction angle combined with slab rollback events, which

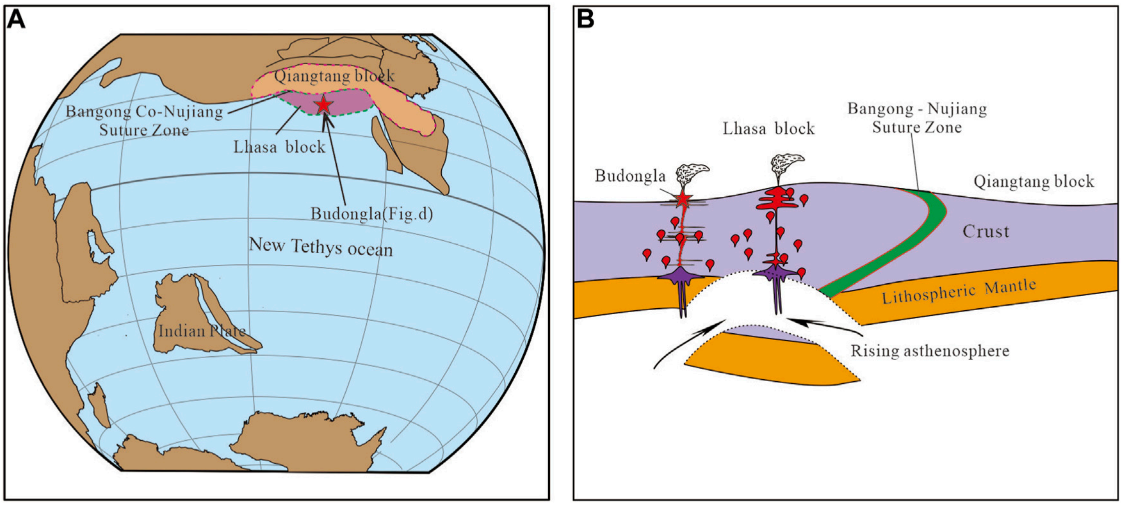

FIGURE 9
Schematic illustrations of the Late Cretaceous tectono-magmatic evolution of the Qiangtang-Lhasa terrane. [**(A)**, Basemap after Ma et al., 2014 **(B)**, Basemap after Zhu et al., 2016].

triggered the Late Cretaceous magmatism (Zhang et al., 2012; Zhang et al., 2015); and still other scholars believed that the northward subduction of the Yarlung Zangbo Neotethys Ocean was normal deep subduction and that slab breakoff events triggered the Late Cretaceous magmatic episodes (Dai et al., 2020). In the low-angle subduction model, the early subduction angle was small, and the corresponding magmatism was slight. However, in recent years, extensive Jurassic-Cretaceous magmatism has been found in the southern Lhasa terrane (Zhu et al., 2011; Liu et al., 2019c), which is contrary to the low-angle subduction model of the oceanic plate. Considering that the Lhasa terrane experienced significant crustal shortening after Cretaceous time, the distance between the northern magmatic arc and the southern Neotethyan subduction zone was more than 600 km (Ding and Lai, 2003; Kapp et al., 2007), which cannot be explained by the normal subduction model. Therefore, we believe that the 90 Ma magmatism in the Central Lhasa terrane was unlikely to have been related to the subduction of the Yarlung Zangbo oceanic lithosphere.

The magmatism of the Lhasa terrane was mainly influenced by the evolution of the Yarlung Zangbo Ocean and Bangong-Nujiang Ocean (Chen et al., 2014; Zheng et al., 2014). Currently, no consensus has been reached on the timing of tectonic evolution and subduction polarity of the Bangong-Nujiang suture zone (Kapp et al., 2005; Volkmer et al., 2007; Li G. M. et al., 2011; Gao et al., 2011; Geng et al., 2011; Li H. L. et al., 2014; Wang et al., 2016; Zhu et al., 2016): some scholars have proposed that the Bangong-Nujiang ocean basin subducted northward beneath the Qiangtang block in the Early Jurassic, while the arc-arc "soft" collision between the Lhasa and Qiangtang blocks is most likely to have occurred between 140 Ma and 130 Ma (Song et al., 2019); at the same time, the Nyima area in the Northern Lhasa terrane records a 125–118 Ma transition from marine facies to nonmarine facies (Kapp et al., 2007), and it was an intracontinental environment at approximately 110 Ma, which means that the Lhasa and Qiangtang blocks underwent a "soft" collision before 110 Ma (Zhu et al., 2009). Other scholars have proposed that the large-scale magmatic activity at approximately 113 Ma around Xainza in the middle of the Central Lhasa terrane was the product of the southward subduction of the Bangong-Nujiang ocean slab breakoff (Chen et al., 2014). In addition, the appearance of the large-scale Jingzhushan formation (K_{2j}) molasse in the BNSZ also suggests that the Lhasa terrane in the later part of the Early Cretaceous had entered the continental collision stage (Pan et al., 2006). Thus, the above lines of evidence fully show that the Bangong-Nujiang Ocean in the Nyima-Bange area had closed and entered a state of collisional orogeny by the middle-late part of the Early Cretaceous.

Similar to Balaza, Sebuta, Ga'erqiong, Jianglaangzong, and many other ca. 90 Ma intermediate-felsic intrusions in the Central Lhasa subterrane (Ouyang et al., 2017; Dai et al., 2020), the intermediate-felsic pluton in Budongla was formed in a post-collisional environment (Figures 8C,D). Based on the results of the above discussion, we believe that the ~90 Ma magmatism and mineralization in the Central Lhasa subterrane are not the products of melting of subducted seafloor or ocean ridge subduction of the Yarlung-Zangbo Ocean or southward subduction of the Bangong-Nujiang Ocean.

According to the analysis above, by the later part of the Early Cretaceous, the Bangong-Nujiang ocean basin had closed, and the central and northern parts of the Lhasa terrane had entered the stage of continental collision. During the disappearance of the Bangong-Nujiang oceanic crust, mantle material upwelling caused mantle-derived magma underplating to occur at an unequal scale on either side of the Bangong-Nujiang junction zone (Zhu, et al., 2016). Subsequently, the lower crust of the Central Lhasa subterrane was continuously thickened due to the compression of north-south stress. And its thickness was greater than 50 km (Dai et al., 2020). At this time, the ultrahigh-pressure metamorphism occurred at the bottom of the crust, reaching eclogite facies (Li J. X. et al., 2011; Sun et al., 2015; Ding et al., 2016). During the Late Cretaceous period, this thickened crust underwent delamination (Yu et al., 2011; Liu et al., 2018c), which led to a series of ~90 Ma magmatic episodes, such as the event that produced the Budongla pluton (Figures 9A,B).

Conclusion

(i) The formation age of the monzodiorite pluton of the Budongla gold district in the western part of the Central Lhasa subterrane is 92.7 ± 1.1 Ma, and this pluton is the product of Late Cretaceous magmatism in the Central Lhasa subterrane.

(ii) The monzodiorite of the Budongla gold district in the western part of the Central Lhasa subterrane belongs to the metaluminous, high-K calc-alkaline Mg-rich intermediate-felsic magmatic series, and the Budongla monzodiorite was emplaced during the post-collisional period of the Lhasa terrane and the Qiangtang terrane.

Data availability statement

The original contributions presented in the study are included in the article/supplementary material, further inquiries can be directed to the corresponding authors.

Author contributions

Conceptualization, HL; software, J-YW; investigation, HL, D-FM, YO, H-XH, Z-LZ, and TL; data curation, HL; writing—original draft preparation, HL; writing—review and editing, HL and Y-GL; visualization, HL; supervision, H-XH; project admin-istration, W-CL and G-ML; funding acquisition, W-CL and G-ML. All authors have read and agreed to the published version of the manuscript.

Funding

Key Programme, National Natural Science Foundation of China (No. 92055314 and 91955208); the National Key R and D Program of China (Grant Numbers: 2021YFC2901803; 2019YFC0605201, and 2021YFC2901903), China Geological Survey Project (Grant Numbers: DD20221776; DD20190542, and DD20190147); Tianfu ten thousand talents program outstanding scientists project (No. 023).

Acknowledgments

The authors of this paper are very grateful to Associate Professor He Xiaohu from Yunnan University, Associate Professor Gao Sunbao, China University of Geosciences (Wuhan); Senior Engineer Liu Han, Senior Engineer Zhang Zhi, senior engineer Wang Yiyun, Professor Zhu Xiangping, Chengdu Center, China Geological Survey; Senior Engineer Liu Chaoqiang, Senior Engineer Li Yanbo, Engineer Yao Bo, Engineer Liu Huadong, the fifth Geological Team of Xizang Geological Exploration Bureau.

Conflict of interest

The authors declare that the research was conducted in the absence of any commercial or financial relationships that could be construed as a potential conflict of interest.

The reviewer JZ declared a shared affiliation with the author JW to the handling editor at the time of review.

Publisher's note

References

Blichert-Toft, J., and Albarède, F. (1997). The Lu-Hf isotope geochemistry of chondrites and the evolution of the mantle-crust system. *Earth Planet. Sci. Lett.* 148 (1–2), 243–258. doi:10.1016/S0012-821X(97)00040-X

Boztuğ, D., Harlavan, Y., Arehart, G., Satir, M., and Avci, N. (2007). K-Ar age, whole-rock and isotope geochemistry of A-type granitoids in the Divriği-Sivas region, Eastern-Central Anatolia, Turkey. *Lithos* 97, 193–218. doi:10.1016/j.lithos.2006.12.014

Cao, H. W., Zhang, Y. H., Santosh, M., Li, G. M., Hollis, S. P., Zhang, L. K., et al. (2019). Petrogenesis and metallogenic implications of cretaceous magmatism in central Lhasa, Tibetan plateau: A case study from the lunggar Fe skarn deposit and perspective review. *Geol. J.* 54 (4), 2323–2346. doi:10.1002/gj.3299

Cai, Q. L., Zheng, Z. W., and He, J., (2015). Age of zircon U-Pb and its geological significance of granite from western Gangdese in Tibet. *J. East China Inst. of*

Technol. 38 (1), 49–57. (in Chinese with English abstract). doi:10.3969/j.issn.1674-3504.2015.01.007

Chen, Y., Zhu, D. C., Zhao, Z. D., Meng, F. Y., Wang, Q., Santosh, M., et al. (2014). Slab breakoff triggered ca.113Ma, magmatism around Xainza area of the Lhasa terrane, Tibet. *Gondwana Res.* 26 (2), 449–463. doi:10.1016/j.gr.2013.06.005

Dai, Z. W., Huang, H. X., Li, G. M., Huizenga, J. M., Santosh, M., Cao, H. W., et al. (2020). Formation of Late Cretaceous high-Mg granitoid porphyry in central Lhasa, Tibet: Implications for crustal thickening prior to India–Asia collision. *Geol. J.* 55, 6696–6717. doi:10.1002/gj.3834

Ding, H. X., Hou, Q. Y., and Zhang, Z. M. (2016). Petrogenesis and tectonic significance of the eocene adakite-like rocks in Western Yunnan, southeastern Tibetan plateau. *Lithos* 245, 161–173. doi:10.1016/j.lithos.2015.09.024

Ding, L., and Lai, Q. Z. (2003). New geological evidence of crustal thickening in the Gangdese block prior to the Indo-Asian collision. *Chin. Sci.*, 1610–1616. doi:10.1360/02wd0586

Gao, S. B. (2016). *Copper-iron polymetal metallogenic regularity and election of Targeet areas in the western of Gangdise metallogenic belt, Tibet*. Ph. D thesis. Wuhan: China University of Geosciences, 16. (in Chinese with English abstract).

Gao, S. B., Zheng, Y. Y., Wang, J. S., Zhang, Z., and Yang, C. (2011). The geochronology and geochemistry of intrusive rocks in Bange area: Constraints on the evolution time of the Bangong Lake - nujiang ocean basin. *Acta Petrol. Sin.* 27 (7), 1973–1982. (in Chinese with English abstract).

Geng, Q. R., Li, W. C., Wang, L. Q., Zeng, X. T., Peng, Z. M., Zhang, X. F., et al. (2021). Paleozoic tectonic framework and evolution of the central and western Tethys. *Sediment. Geol. Tethyan Geol.* 41 (2), 297–315. (in Chinese with English abstract). doi:10.19826/j.cnki.1009-3850.2021.02012

Geng, Q. R., Pan, G. T., Wang, L. Q., Peng, Z. M., and Zhang, Z. (2011). Tethyan evolution and metallogenic geological background of the Bangong Co–Nujiang belt and the Qiangtang massif in Tibet. *Geol. Bull. China* 30 (8), 1261–1274. (in Chinese with English abstract).

Griffin, W. L., Pearson, N. J., Belousova, E., Jackson, S. E., Achterbergh, E. V., O'Reilly, S. Y., et al. (2000). The Hf isotope composition of cratonic mantle: LAM-MC-ICPMS analysis of zircon megacrysts in kimberlites. *Geochim. Cosmochim. Acta* 64, 133–147. doi:10.1016/s0016-7037(99)00343-9

Griffin, W. L., Wang, X., Jackson, S. E., Pearson, N. J., O'Reilly, S. Y., Xu, X. S., et al. (2002). Zircon chemistry and magma mixing, SE China: In–situ analysis of Hf isotopes, tonglu and pingtan igneous complexes. *Lithos* 61, 237–269. doi:10.1016/s0024-4937(02)00082-8

Grimes, C. B., John, B. E., Kelemen, P. B., Mazdab, F. K., Wooden, J. L., Cheadle, M. J., et al. (2007). Trace element chemistry of zircons from oceanic crust: A method for distinguishing detrital zircon provenance. *Geol.* 35 (7), 643–646. doi:10.1130/g23603a.1

Hoskin, P., and Black, L. P. (2000). Metamorphic zircon formation by solid-state recrystallization of protolith igneous zircon. *J. Metamorph. Geol.* 18 (4), 423–439. doi:10.1046/j.1525-1314.2000.00266.x

Hoskin, P. W. O. (2005). Trace-element composition of hydrothermal zircon and the alteration of Hadean zircon from the Jack Hills, Australia. *Geochim. Cosmochim. Acta* 69, 637–648. doi:10.1016/j.gca.2004.07.006

Hou, Z. Q., Yang, Z. M., Lu, Y. J., Kemp, A., Zheng, Y. C., Li, Q. Y., et al. (2015). A genetic linkage between subduction- and collision-related porphyry Cu deposits in continental collision zones. *Geology* 43, 247–250. doi:10.1130/g36362.1

Huang, H. X., Dai, Z. W., Liu, H., Chen, M. H., Li, G. M., Cao, H. W., et al. (2021b). Hydrothermal zircon dating of Shangxu gold deposit in Tibet and restriction on the Early Cretaceous orogenic gold mineralization in the middle Bangonghu–Nujiang suture zone. *Acta Geol. Sin. Engl. Ed.* 95 (4), 1249–1259. doi:10.1111/1755-6724.14679

Huang, H. X., Dai, Z. W., Liu, H., Li, G. M., Huizenga, J. M., Zhang, L. K., et al. (2021a). Zircon U–Pb ages, geochemistry, and Sr–Nd–Pb–Hf isotopes of the mugagangri monzogranite in the southern Qiangtang of Tibet, Western China: Implications for the evolution of the bangong Co-nujiang meso-Tethyan Ocean. *Geol. J.* 56, 3170–3186. doi:10.1002/gj.4094

Huang, H. X., Li, G. M., Dong, S. L., Liu, B., Zhang, H., Zhang, L., et al. (2012b). SHRIMP zircon U-Pb age and geochemical characteristics of Qinglung, granodiorite in Baingoin area, Tibet. *Geol. Bull. China* 31 (6), 852–859. (in Chinese with English abstract).

Huang, H. X., Li, G. M., Liu, H., Cao, H. W., and Zhang, Z. L. (2018a). Zircon U-Pb age of the shangxu gold deposit from bangong - nujiang Co, northern Tibet, and restriction on the early cretaceous orogenic gold mineralisation. *Acta Geol. Sin. - Engl. Ed.* 92 (4), 1664–1666. doi:10.1111/1755-6724.13657

Huang, H. X., Li, G. M., Zeng, Q. G., Liu, B., Duan, Z. M., Dong, S. L., et al. (2012a). Geochronology of the Chagele Pb-Zn deposit in Tibet and its significance. *Geol. China* 39 (3), 750–759. (in Chinese with English abstract).

Huang, Y., Cao, H. W., Li, G. M., Brueckner, S. M., Zhang, Z., Dong, L., et al. (2018b). Middle-late triassic bimodal intrusive rocks from the Tethyan Himalaya in south Tibet: Geochronology, petrogenesis, and tectonic implications. *Lithos* 318–319, 78–90. doi:10.1016/j.lithos.2018.08.002

Huang, Y., Li, G. M., Ding, J., Dai, J., Yan, G. Q., Dong, S. L., et al. (2017). Origin of the newly discovered Zhunuo porphyry Cu-Mo-Au deposit in the Western part of the Gangdese porphyry copper belt in the southern Tibetan plateau, SW China. *Acta Geol. Sin. - Engl. Ed.* 91 (1), 109–134. doi:10.1111/1755-6724.13066

Huang, Y., Ren, M. H., Jowitt, S. M., Li, G. M., Fu, J. G., Lang, X. H., et al. (2021c). Middle triassic arc magmatism in the southern Lhasa terrane: Geochronology, petrogenesis, and tectonic setting. *Lithos* 380-381, 105857. doi:10.1016/j.lithos.2020.105857

Huang, Y., Ren, M. H., Liang, W., Li, G. M., Heilbronn, K., Dai, Z. W., et al. (2020). Origin of the oligocene Tuolangla porphyry-skarn Cu-W-Mo, deposit in Lhasa terrane, southern Tibet. *China Geol.* 3, 369–384. doi:10.31035/cg2020047

Kapp, P., DeCelles, P. G., Gehrels, G. E., Heizler, T. M., and Ding, L. (2007). Geological records of the Lhasa-Qiangtang and Indo-Asian collisions in the Nima area of central Tibet. *Geol. Soc. Am. Bull.* 119 (7–8), 917–933. doi:10.1130/b26033.1

Kapp, P., Yin, A., Harrison, T. M., and Ding, L. (2005). Cretaceous-Tertiary shortening, basin development, and volcanism in Central Tibet. *Geol. Soc. Am. Bull.* 117 (7–8), 865–878. doi:10.1130/b25595.1

LeMaitre, R. W. (2002). *Igneous rocks: A classification and glossary of terms*. Cambridge: Cambridge University Press, 3–42.

Li, G. M., Duan, Z. M., Liu, B., Zhang, H., Dong, S. L., and Zhang, L. (2011). The discovery of Jurassic accretionary complexes in Duolong area, northern Bangong Co - Nujiang suture zone, Tibet, and its geologic significance. *Geol. Bull. China* 30 (8), 1256–1260. (in Chinese with English abstract).

Li, H. L., Gao, C., Li, Z. H., Zhang, Z., Peng, Z. M., and Guan, J. L. (2016). Age and tectonic significance of Jingzhushan formation in bangong lake area, Tibet. *Geotect. Metallogenia* 40 (3), 535–542. (in Chinese with English abstract).

Li, H. L., Yang, S., Li, D. W., Zhang, S., Lü, Z. W., and Chen, G. F. (2014). Geochronology, geochemistry, tectonic setting, and metallogenetic significance of the Late Cretaceous quartz monzonite in the northwestern, Gangdise terrane. *Geotect. Metallogenia* 38 (3), 694–705. (in Chinese with English abstract).

Li, J. X., Qin, K. Z., Li, G. M., Richards, J. P., Zhao, J. X., and Cao, M. J. (2014). Geochronology, geochemistry, and zircon Hf isotopic compositions of Mesozoic intermediate–felsic intrusions in central Tibet: Petrogenetic and tectonic implications. *Lithos* 198, 77–91. doi:10.1016/j.lithos.2014.03.025

Li, J. X., Qin, K. Z., Li, G. M., Xiao, B., Chen, L., and Zhao, J. X. (2011). Post-collisional ore-bearing adakitic porphyries from gangdese porphyry copper belt, southern Tibet: Melting of thickened juvenile arc lower crust. *Lithos* 126 (3–4), 265–277. doi:10.1016/j.lithos.2011.07.018

Li, Y. C., Huang, H. X., Liu, H., and Lan, S. S. (2017). Gold mineralization in the Bangong lake-Nujiang metallogenic zone, Xizang. *Sediment. Geol. Tethyan Geol.* 37 (2), 1–13. (in Chinese with English abstract).

Liu, H., Huang, H. X., Li, G. M., Li, W. C., Li, Y. G., Ma, D. F., et al. (2022a). Petrogenesis of an Early Cretaceous Xiabie Co I-type granite in southern Qiangtang, Tibet: Evidence from geochemistry, geochronology, Rb-Sr, Sm-Nd, Lu-Hf and Pb isotopes. *Acta Geol. Sin. Engl. Ed.* 96 (3), 919–937. doi:10.1111/1755-6724.14777

Liu, H., Huang, H. X., Li, G. M., Xiao, W. F., Zhang, Z. L., Liu, B., et al. (2015). Factor analysis in geochemical survey of the Shangxu gold deposit, northern Tibet. *Geol. China* 42 (4), 1126–1136. (in Chinese with English abstract).

Liu, H., Huang, H. X., Zhang, L. K., Li, G. M., Lü, M. H., Yan, G. Q., et al. (2019a). Origin and evolution of Ore–Forming fluids in Luerma porphyry copper deposit from the Western Gangdise. *Earth Sci.* 44 (6), 1935–1956. (in Chinese with English abstract). doi:10.3799/dqkx.2018.370

Liu, H., Huang, H. X., Zhang, L. K., Li, G. M., Ouyang, Y., Huang, Y., et al. (2021a). Luerma, a newly discovered Late Triassic porphyry copper-gold ore-spot in the Western Gangdise metallogenic belt, Tibet. *Sediment. Geol. Tethyan Geol.* 41 (4), 599–611. (in Chinese with English abstract). doi:10.19826/j.cnki.1009-3850.2020.06001

Liu, H., Li, F. Q., Zhou, F., Li, J., Gou, Z. B., Yang, Y., et al. (2018c). Late paleozoic earthquake events in the Nixiong area and its geological significance, western Lhasa block. *Earth Sci.* 43 (8), 2767–2779. doi:10.3799/dqkx.2018.167

Liu, H., Li, G. M., Huang, H. X., Cao, H. W., Yuan, Q., Li, Y. X., et al. (2018a). Petrogenesis of late cretaceous jiangla'angzong I-type granite in central Lhasa terrane, Tibet, China: Constraints from whole-rock geochemistry, zircon U-Pb geochronology, and Sr-Nd-Pb-Hf isotopes. *Acta Geol. Sin. - Engl. Ed.* 92 (4), 1396–1414. doi:10.1111/1755-6724.13634

Liu, H., Li, G. M., Huang, H. X., Xiao, W. F., Yan, G. Q., Ma, D. F., et al. (2018b). Sources of ore-forming materials in the Shangxu orogenic gold deposit, northern Xizang (Tibet), constraints form C., S., and Pb isotopes. *Geol. Rev.* 64 (5), 1285–1301. (in Chinese with English abstract).

Liu, H., Li, G. M., Huang, H. X., Zhang, L. K., Lan, S. S., Fu, J. G., et al. (2019b). Sources of ore–forming materials of Luerma porphyry copper (gold) deposit, Western Gangdise. *Mineral. Deposits* 38 (4), 631–643. (in Chinese with English abstract). doi:10.16111/j.0258-7106.2019.03.012

Liu, H., Li, G. M., Huang, H. X., Zhang, L. K., Lü, M. H., Lan, S. S., et al. (2019c). The discovery of the Late Triassic porphyry type Cu deposit from Gangdise metallogenic belt, Tibet. *Geol. China* 46 (5), 1238–1240. (in Chinese with English abstract). doi:10.12029/gc20190524

Liu, H., Li, G. M., Huang, H. X., Zhang, Z. L., Xiao, W. F., Jiao, Y. J., et al. (2017). Prospecting potential analysis of deep No. III ore section in the Shangxu orogenic Gold deposit, bangong Co–Nujiang metallogenic belt, Tibet. *Acta Geol. Sin.* 91 (6), 1245–1258. (in Chinese with English abstract).

Liu, H., Li, G. M., Li, W. C., Huang, H. X., Li, Y. G., Ouyang, Y., et al. (2022b). Petrogenesis and tectonic setting of the late Early Cretaceous Kong Co A-type granite in the northern margin of Central Lhasa subterrane, Tibet. *Acta Petrol. Sin.* 38 (1), 230–252. (in Chinese with English abstract). doi:10.18654/1000-0569/2022.01.15

Liu, H., Li, G. M., Li, W. C., Zhang, J. H., Li, Y. G., Zhang, Z. L., et al. (2021b). Epithermal mineralization at Budongla gold deposit in Zhongba County of Tibet: Evidence from fluid inclusions and H–O isotopes. *Mineral. Deposits* 40 (2), 311–328. (in Chinese with English abstract). doi:10.16111/j.0258-7106.2021.02.008

Liu, H., Zhang, H., Li, G. M., Huang, H. X., Xiao, W. F., You, Q., et al. (2016). Petrogenesis of the early cretaceous Qingcaoshan strongly peraluminous S–type granitic pluton, southern Qiangtang, northern Tibet: Constraints from whole–rock geochemistry and zircon U–Pb geochronology. *Acta Sci. Nat. Univ. Pekin.* 52 (5), 848–860. (in Chinese with English abstract). doi:10.13209/j.0479-8023.2016.045

Liu, H., Zhang, L. K., Huang, H. X., Li, G. M., Ouyang, Y., Yu, H., et al. (2020). Evolution of ore–forming fluids in the Luobuzhen epithermal gold–silver deposit in Western gangdisi: Fluid inclusion and H–O isotope evidence. *Earth Sci. Front.* 27 (4), 49–65. (in Chinese with English abstract). doi:10.13745/j.esf.sf.2020.4.23

Ma, Y. M., Yang, T. S., Yang, Z. Y., Zhang, S. H., Wu, H. C., Li, H. Y., et al. (2014). Paleomagnetism and U-Pb zircon geochronology of lower cretaceous lava flows from the Western Lhasa terrane: New constraints on the India-Asia collision process and intracontinental deformation within Asia. *J. Geophys. Res. Solid Earth* 119, 7404–7424. doi:10.1002/2014jb011362

Maniar, P. D., and Piccoli, P. M. (1989). Tectonic discrimination of granitoids. *Geol. Soc. Am. Bull.* 101, 635–643. doi:10.1130/0016-7606(1989)101<0635:tdog>2.3.co;2

McDonough, W. F., and Sun, S. S. (1995). The composition of the Earth. *Chem. Geol.* 120, 223–253. doi:10.1016/0009-2541(94)00140-4

McKenzie, D., and Bickle, M. (1988). The volume and composition of melt generated by extension of the lithosphere. *J. Petrology* 29, 625–679. doi:10.1093/petrology/29.3.625

Meng, F. Y., Zhao, Z. D., Zhu, D. C., Mo, X. X., Guan, Q., Huang, Y., et al. (2014). Late cretaceous magmatism in mamba area, central Lhasa subterrane: Products of back-arc extension of Neo-Tethyan Ocean? *Gondwana Res.* 26 (2), 505–520. doi:10.1016/j.gr.2013.07.017

Middlemost, E. A. K. (1994). Naming materials in the magma/igneous rock system. *Earth Sci. Rev.* 37, 215–224. doi:10.1016/0012-8252(94)90029-9

Ouyang, Y., Yang, W. N., Huang, H. X., Liu, H., Zhang, J. L., and Zhang, J. H. (2017). Metallogenic dynamics background of Ga'erqiong Cu-Au deposit in Tibet, China. *Earth Sci. Res. J.* 21 (2), 59–65. doi:10.15446/esrj.v21n2.65192

Ouyang, Y., Zhao, Y. B., Ni, Z. Y., Zhang, J. H., and Gao, H. (2016). Alteration remote sensing anomaly extraction in Jiangla'angzong area of Tibet. *Remote Sens. Inf.* 31 (5), 90–95. (in Chinese with English abstract).

Pan, G. T., Mo, X. X., Hou, Z. Q., Zhu, D. C., Wang, L. Q., Li, G. M., et al. (2006). Spatial–temporal framework of the Gangdese orogenic belt and its evolution. *Acta Petrol. Sin.* 22 (3), 521–533. (in Chinese with English abstract). doi:10.3321/j.issn:1000-0569.2006.03.001

Pan, G. T., Wang, L. Q., Li, X. Z., Wang, J. M., and Xu, Q. (2001). The tectonic framework and spatial allocation of the archipelagic arc–basin systems on the Qinghai-Xizang Plateau. *Sediment. Geol. Tethyan Geol.* 21 (3), 1–26. (in Chinese with English abstract).

Pan, G. T., Xiao, Q. H., Lu, S. N., Deng, J. F., Feng, Y. M., Zhang, K. X., et al. (2009). Subdivision of tectonic units in China. *Geol. China* 36 (1), 1–28. (in Chinese with English abstract).

Pan, G. T., Wang, L. Q., Yin, F. G., Geng, Q. R., Li, G. M., and Zhu, D. C. (2022). Researches on geological-tectonic evolution of Tibetan Plateau: A review, recent advances, and directions in the future. *Sediment. Geol. Tethyan Geol.* 42 (2), 151–175. (in Chinese with English abstract). doi:10.19826/j.cnki.1009-3850.2022.05004

Pearce, J. A., Harris, N. B. W., and Tindle, A. G. (1984). Trace element discrimination diagrams for the tectonic interpretation of granitic rocks. *J. Petrology* 25, 956–983. doi:10.1093/petrology/25.4.956

Peng, J. H., Zhao, L. X., He, J., Huang, S. C., and Gong, C., (2013). Discovery of Indosinian magmatic rocks and its significance in western Gangdise, Tibet. J. East China Inst. *Technol.* 36 (6), 21–26. (in Chinese with English abstract). doi:10.3969/j.issn.1674-3504.2013.s2.004

Qin, Z., Yang, Z. J., Tang, L., Wang, M. Z., Yu, P. T., Han, K., et al. (2019). Geochemical characteristics, zircon U-Pb age and metallogenic significance of Chalong granites in the Gangdise Belt of Tibet. *Geol. Bull. China* 38 (2–3), 231–241. (in Chinese with English abstract).

Scherer, E. E., Cameron, K. L., and Blichert, J. (2000). Lu–hf garnet geochronology: Closure temperature relative to the Sm–Nd system and the effects of trace mineral inclusions. *Geochimica Cosmochimica Acta* 64, 3413–3432. doi:10.1016/s0016-7037(00)00440-3

Song, Y., Zeng, Q. G., Liu, H. Y., Liu, Z. B., Li, H. F., and De, Y. Z. (2019). An innovative perspective for the evolution of bangong–Nujiang Ocean: Also discussing the paleo- and neo-tethys conversion. *Acta Petrol. Sin.* 35 (3), 625–641. (in Chinese with English abstract). doi:10.18654/1000-0569/2019.03.02

Sun, G. Y., Hu, X. M., Zhu, D. C., Hong, M. T., Wang, J. G., and Wang, Q. (2015). Thickened juvenile lower crust–derived ~90 Ma, adakitic rocks in the Central Lhasa terrane, Tibet. *Lithos* 224–225, 225–239. doi:10.1016/j.lithos.2015.03.010

Sun, S. S., and MchDonough, W. F. (1989). Chemical and isotopic systematics of oceanic basalts: Implication for mantle composition and processes. *Geol. Soc. Spec. Pulication* 42, 303–345. doi:10.1144/GSL.SP.1989.042.01.19

Tang, J. X., Sun, X. G., Din, G. S., Wang, Q., Wang, Y. Y., Yang, C., et al. (2014). Discovery of the epithermal deposit of Cu (Au-Ag) in the Duolong ore concentrating area, Tibet. *Adv. Earth Sci.* 35 (1), 6–10. (in Chinese with English abstract). doi:10.3975/cagsb.2014.01.02

Taylor, S. R., and McLennan, S. M. (1985). *The continental crust: Its composition and evolution*. Oxford: Blackwell Scientific Publications, 0–312.

Volkmer, J. E., Kapp, P., Guyn, N. J. H., and Lai, Q. (2007). Cretaceous–tertiary structural evolution of the North central Lhasa terrane, Tibet. *Tectonics* 26, 6007. doi:10.1029/2005tc001832

Wang, B. D., Guo, L., Wang, L. Q., Li, B., Huang, H. X., Chen, F. Q., et al. (2012). Geochronology and petrogenesis of the ore–bearing pluton in Chagele deposit in middle of the Gangdese metallogenic belt. *Acta Petrol. Sin.* 28 (5), 1647–1662. (in Chinese with English abstract).

Wang, B. D., Wang, L. Q., Chung, S. L., Chen, J. L., Yin, F. G., Liu, H., et al. (2016). Evolution of the Bangong–Nujiang Tethyan ocean: Insights from the geochronology and geochemistry of mafic rocks within ophiolites. *Lithos* 245, 18–33. doi:10.1016/j.lithos.2015.07.016

Wang, B. D., Xu, J. F., Liu, B. M., Chen, J. L., Wang, L. Q., Guo, L., et al. (2013). Geochronology and ore-forming geological background of 90 Ma, porphyry copper deposit in the Lhasa terrane, Tibet plateau. *Acta Geol. Sin.* 87 (1), 71–80. (in Chinese with English abstract).

Wang, X. X., Yan, G. Q., Liu, H., Huang, H. X., Lai, Y., Tian, S. Y., et al. (2021b). The genesis of the late cretaceous qusang'gele granitie in central Lhasa terrane, Tibet: Constraints by geochemistry, zircon U-Pb geochronology, and Sr-Nd-Pb-Hf isotopes. *Earth Sci.* 46 (8), 2832–2849. (in Chinese with English abstract). doi:10.3799/dqkx.2020.278

Wang, L. Q., Wang, B. D., Li, G. M., Wang, D. B., and Peng, Z. M. (2021a). Major progresses of geological survey and research in East Tethys: An overview. *Sediment. Geol. Tethyan Geol.* 41 (2), 283–296. (in Chinese with English abstract). doi:10.19826/j.cnki.1009-3850.2021.01008

Wang, Q., Pan, G. T., Tang, F. W., Yang, J., Xia, S. B., Zhang, W., et al. (2022). Basic features of crust-mantle structure of the Tibet Plateau. *Sediment. Geol. Tethyan Geol.* 42 (2), 319–329. (in Chinese with English abstract). doi:10.19826/j.cnki.1009-3850.2022.04016

Wu, H. H., Zhang, G. Q., and Wang, W., (2017). U-Pb dating of Chromite from Shannan Jinluxi in Tibet and its Geological Significance. J. East China Inst. *Technol.* 40 (3), 246–252. (in Chinese with English abstract). doi:10.3969/j.issn.16743504.2017.03.005

Xu, Z. Q., Yang, J. S., Li, W. C., Li, H. Q., Cao, Z. H., Yan, Z., et al. (2013). Paleo–Tethys system and accretionary orogen in the Tibet plateau. Acta Petrol. Sin. 29 (6), 1847–1860. (in Chinese with English abstract).

Yan, L. L., and Zhang, K. J. (2020). Infant intra-oceanic arc magmatism due to initial subduction induced by oceanic plateau accretion: A case study of the bangong meso-tethys, central Tibet, Western China. *Gondwana Res.* 79, 110–124. doi:10.1016/j.gr.2019.08.008

Yang, J. S., Xu, Z. Q., Li, T. F., Li, H. Q., Li, Z. L., Ren, Y. F., et al. (2007). Oceanic subduction–type eclogite in the Lhasa terrane, Tibet, China: Remains of the paleo–tethys Ocean basin? *Geol. Bull. China* 26 (10), 1277–1287. (in Chinese with English abstract).

Yu, H. X., Chen, J. L., Xu, J. F., Wang, B. D., Wu, J. B., and Liang, H. Y. (2011). Geochemistry and origin of late cretaceous (-90Ma) ore-bearing porphyry of balazha in mid-northern Lhasa terrane, Tibet. *Acta Petrol. Sin.* 27 (7), 2011–2022. (in Chinese with English abstract).

Zhang, K. J., Li, Q. H., Yan, L. L., Lu, L. Z., Zhang, Y. X., Hui, J., et al. (2017). Geochemistry of limestones deposited in various plate tectonic settings. *Earth-Science Rev.* 167, 27–46. doi:10.1016/j.earscirev.2017.02.003

Zhang, K. J., Zhang, Y. X., Tang, X. C., and Xia, B. (2012). Late Mesozoic tectonic evolution and growth of the Tibetan plateau prior to the Indo-Asian collision. *Earth-Science Rev.* 114 (3–4), 236–249. doi:10.1016/j.earscirev.2012.06.001

Zhang, Z., Yao, X., Tang, J., Li, Z. J., Wang, L. Q., Yang, Y., et al. (2015). Litho geochemical, Re-Os and U-Pb geochronological, Hf-Lu and S-Pb isotope data of the Ga'erqiong-galale Cu-Au ore-concentrated area: Evidence for the late cretaceous magmatism and metallogenic event in the bangong–nujiang suture zone, northwestern Tibet. *Resour. Geol.* 65 (2), 76–102. doi:10.1111/rge.12064

Zhao, Y. Y., Cui, Y. B., Lü, L. L., and Shi, D. H. (2011). Chronology, geochemical characteristics and the significance of Shesuo copper polymetallic deposit, Tibet. *Acta Petrol. Sin.* 27 (7), 2132–2142. (in Chinese with English abstract).

Zhao, L. X., Gong, C., He, J., Peng, J. H., Huang, S. C., and Yang, Z. L., (2013). Discovery of porphyry copper deposit and its significance of Dajiacuo in Cuoqin County, Tibet. *J. East China Inst. Technol.* 36 (6), 13–20. (in Chinese with English abstract). doi:10.3969/j.issn.16743504.2013.s2.003

Zheng, Y. C., Hou, Z. Q., Gong, Y. L., Liang, W., Sun, Q. Z., Zhang, S., et al. (2014). Petrogenesis of cretaceous adakite–like intrusions of the gangdese plutonic belt, southern Tibet: Implications for mid-ocean ridge subduction and crustal growth. *Lithos* 190–191, 240–263. doi:10.1016/j.lithos.2013.12.013

Zhu, D. C., Li, S. M., Cawood, P. A., Wang, Q., Zhang, Z. D., Liu, S., et al. (2016). Assembly of the Lhasa and Qiangtang terranes in central Tibet by divergent double subduction. *Lithos* 245, 7–17. doi:10.1016/j.lithos.2015.06.023

Zhu, D. C., Mo, X. X., Niu, Y. L., Zhao, Z. D., Wang, L. Q., Liu, Y. S., et al. (2009). Geochemical investigation of Early Cretaceous igneous rocks along an east-west traverse throughout the Central Lhasa terrane, Tibet. *Chem. Geol.* 268, 298–312. doi:10.1016/j.chemgeo.2009.09.008

Zhu, D. C., Zhao, Z. D., Niu, Y. L., Mo, X. X., Chung, S. L., Hou, Z. Q., et al. (2011). The Lhasa terrane: Record of a microcontinent and its histories of drift and growth. *Earth Planet. Sci. Lett.* 301 (1), 241–255. doi:10.1016/j.epsl.2010.11.005